

www.acsnano.org

Controlling the Shapes of Nanoparticles by Dopant-Induced Enhancement of **Chemisorption and Catalytic Activity:** Application to Fe-Based Ammonia Synthesis

Qi An,* Molly McDonald, Alessandro Fortunelli,* and William A. Goddard III*



Cite This: ACS Nano 2021, 15, 1675-1684



Read Online

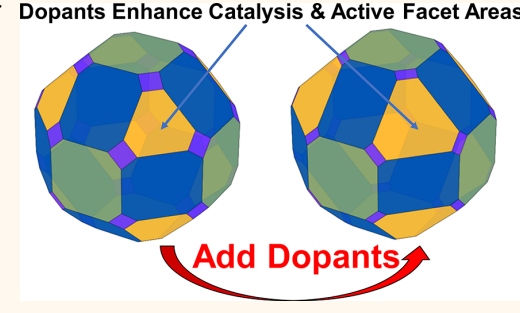
ACCESS I

III Metrics & More

Article Recommendations

Supporting Information

ABSTRACT: We showed recently that the catalytic efficiency of Dopants Enhance Catalysis & Active Facet Areas ammonia synthesis on Fe-based nanoparticles (NP) for Haber-Bosch (HB) reduction of N₂ to ammonia depends very dramatically on the crystal surface exposed and on the doping. In turn, the stability of each surface depends on the stable intermediates present during the catalysis. Thus, under reaction conditions, the shape of the NP is expected to evolve to optimize surface energies. In this paper, we propose to manipulate the shape of the nanoparticles through doping combined with chemisorption and catalysis. To do this, we consider the relationships between the catalyst composition (adding dopant elements) and on how the distribution of the dopant atoms on the bulk and facet sites affects the shape of the particles and therefore the number of active sites on the catalyst surfaces. We use our hierarchical,



high-throughput catalyst screening (HHTCS) approach but extend the scope of HHTCS to select dopants that can increase the catalytically active surface orientations, such as Fe-bcc(111), at the expense of catalytically inactive facets, such as Febcc(100). Then, for the most promising dopants, we predict the resulting shape and activity of doped Fe-based nanoparticles under reaction conditions. We examined 34 possible dopants across the periodic table and found 16 dopants that can potentially increase the fraction of active Fe-bcc(111) vs inactive Fe-bcc(100) facets. Combining this reshaping criterion with our HHTCS estimate of the resulting catalytic performance, we show that Si and Ni are the most promising elements for improving the rates of catalysis by optimizing the shape to decrease reaction barriers. Then, using Si dopant as a working example, we build a steady-state dynamical Wulff construction of Si-doped Fe bcc nanoparticles. We use nanoparticles with a diameter of ~10 nm, typical of industrial catalysts. We predict that doping Si into such Fe nanoparticles at the optimal atomic content of ~0.3% leads to rate enhancements by a factor of 56 per nanoparticle under target HB conditions.

KEYWORDS: nanoparticle, catalyst, wulff construction, dft, high-throughput screening

INTRODUCTION

Metal and metal oxide nanoparticles (NPs), with sizes below 100 nm, are widely used in energy-based research, imaging, medical applications, and catalysis because of their combined chemical and physical properties. 1-6 The morphology of the nanoparticles, in particular their shape, plays a crucial role in determining these properties, which are often surfacedominated. In both fundamental studies and applications, it is typical that specific nanoparticle facets are preferentially desired in order to enhance targeted properties. Thus, many strategies have been devised to manipulate NP shapes via the environment or alloying. For example, the shape of metal NPs is influenced significantly by the reaction conditions. Another

experimental study showed that the shape of palladiumcopper (PdCu) nanocrystal is influenced by the hydrogen pressure.⁸ Another approach is by alloying to change the stable NP surface. In addition, the support for the NPs can also influence the NP shape.10

Received: November 8, 2020 Accepted: December 14, 2020 Published: December 23, 2020





Heterogeneous metal nanoparticle (NP) catalysts often are structure-sensitive, meaning that catalytic reaction rates can vary by orders of magnitude on different surface facets of the same catalyst. 11,12 Since only a fraction of the available NP surface area may exhibit the catalytically most active sites while the rest may remain chemically inert, the relative abundance of the various surface orientations can play an important role in determining the overall kinetics and catalytic efficiency. These issues are captured with the geometric Wulff construction, based on thermodynamics, to predict the equilibrium shapes of nanoparticles from the surface energies of the various facets. This uses a direct proportionality between the surface energy and distance of the facet from the center of mass of the NP. The Wulff construction provides a powerful tool for theoretical analysis of catalysis performance, since it is straightforward to calculate surface energies computationally to predict the extent of each facet as a function of the NP size.

Two issues complicate this task. First, adsorption of reactants on catalyst facets can drastically change surface energetics and hence the Wulff shape of the NPs (a wellestablished phenomenon known as "NP reshaping upon ligand adsorption"). 16 This is taken into account straightforwardly by calculating the free-energy changes upon adsorption of species on each facet at the given thermodynamic conditions and by adding these to modulate the bare surface values, e.g., see refs 17-19. Moreover, it has been shown experimentally and predicted theoretically^{20,21} that, since catalytic processes are not in equilibrium, the state of the catalytic surfaces differs from thermodynamic equilibrium without reactions, so that the actual populations of adsorbates on the surface under given reaction conditions must be used to calculate the stabilization of each facet by ligand adsorption. For example, the aspect ratio of Ag NPs catalyzing propylene epoxidation corresponds to a shape intermediate between those realized when only one reactant (O₂) or only the other (propylene) is present with no reaction occurring.²⁰ In another example, fcc(113) facets develop on Ni NPs during acetylene decomposition because they are specially stabilized by the intermediates of the reaction.²¹ To take this issue into account properly, we previously proposed to use the adsorbate populations from kinetic simulations under steady-state reaction conditions to calculate surface energetics and then to use these modified energetics to generalize the Wulff construction 13,14,22 to a "Wulff construction under steady-state" or "dynamic Wulff construction". 20,23

A second, intriguing phenomenon special to multicomponent or alloyed NPs (or "nanoalloys")^{9,24} involves the propensity of the dopants and reaction intermediates to change under reaction conditions due to differing interactions with the adsorbates.^{25,26} The way this affects facet energetics and hence NP reshaping is complicated by the existence in nanoalloy systems of a combinatorial number of "homotops" (configurations obtained by distributing the different elements over a given structural framework at a fixed composition).^{9,24} In any case, this leads to the phenomena in nanoalloys, such as dependence of the optimal shape upon NP size even at a fixed nanoalloy composition,²⁷ and the dependence of elemental segregation on facet orientation,²⁸ reaction conditions,²⁹ or the support of these phenomena).

A comprehensive view of the interdependence of these different aspects on the prediction of catalytic rates has not been reported. In this work, we illustrate our procedure using ammonia synthesis over Fe-based catalysts (the Haber–Bosch (HB) process) as a specific example, to provide (i) a comprehensive overview linked to catalysis kinetics and (ii) a high-throughput screening protocol, along the lines of our previous hierarchical high-throughput catalyst screening (HHTCS) approach,³³ to select the changes in the catalyst composition (doping) that are most effective to maximize the number of catalytically active reaction sites.

We focus here on the HB process that produces ammonia (NH₃) from nitrogen (N₂) and hydrogen (H₂) gases as a practical example.³⁴ This involves a large number of reaction steps (12-24) but is important for industrial chemistry. NH₃ plays an essential role in the manufacture of fertilizers, explosives, plastics, pesticides, and other chemicals, but it comes with great environmental repercussions: energy-intensity and CO₂ emissions. The industrial HB process consumes ~2% of the world's energy because of the hightemperature, 500-600 °C, and high-pressure, 200-400 atm, conditions.³⁷ Also the complexity of the reaction network for Fe-based catalysts^{23,33} (demonstrated from both experimental³⁸⁻⁴⁰ and theoretical investigations)^{23,41,42} makes HB a realistic example of an industrially relevant catalytic process. Notably, the experimental turnover frequency (TOF) of single crystalline Fe(111) and Fe(211) bcc facets are the two most active surfaces at 673 K and 20 atm total reactant pressure, with TOF more than an order of magnitude higher than Fe(100) and Fe(210) bcc facets and 2 orders of magnitude higher than Fe(110).

We previously applied extensive quantum mechanics (QM) coupled with kinetic Monte Carlo (kMC) simulations to characterize the 24 dominant surface configurations and 12 important reaction barriers for Fe-bcc(111) and Fe-bcc(211) surfaces, from which we derived detailed NH $_3$ formation reaction networks to predict steady-state NH $_3$ turn over frequencies (TOF). ^{23,41} We found TOF = 17.7 NH $_3$ /s (2 × 2) unit-cell on Fe-bcc(111) and 18.7 NH $_3$ /s on Fe-bcc(211) at 400 °C and 20 atm total pressure, in excellent agreement with the experimental TOFs, ^{43,44} demonstrating the accuracy of our QM/kMC approach.

Then, based on the derived reaction network, we developed a hierarchical high-throughput catalyst screening (HHTCS) approach to enable very rapid predictions to identify promising dopants that would dramatically improve reaction rates. ^{33,45-47} For Fe-bcc(111), screening 34 transition metal elements and 18 nontransition metal elements, we identified several candidates (Rh, Pt, Pd, Cu, Ni, Co, and Si) that could increase the overall reaction rates by factors of 4 to ~40. Here we found that the best case is subsurface Si that would be 42 times faster at HB conditions, allowing a substantial reduction in the extreme HB industrial conditions (500 °C, 200 atm) to much milder conditions of either 500 °C at 20 atm or 400 °C at 60 atm while maintaining the same NH₃ production rates as HB on pure Fe-bcc(111).

In this paper, we propose to manipulate the shape of nanoparticles through doping combined with chemisorption and catalysis. We illustrate how to manipulate the particle shape through the doping strategy for Fe-based catalyst aimed at improving the rates for the Haber–Bosch (HB) process, as a specific example to illustrate the principles. Since the industrial Fe catalyst consists of Fe-based NPs, ⁴⁸ the equilibrium NP shape should correspond to a dynamic Wulff construction, ^{13–15,20–23} where the catalytic performance will be maximized if the area of the active Fe-bcc(111) and Fe-

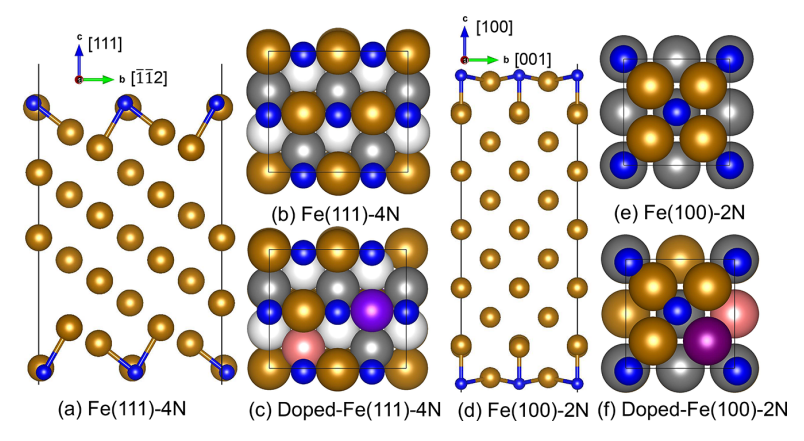


Figure 1. Schematic depictions of Fe-bcc(111) and Fe-bcc(100) surfaces with N adsorption: (a,b) side and top views of the Fe-bcc(111) model, (c) top view of the doped Fe-bcc(111) model, (d,e) side and top views of the Fe-bcc(100) model, and (f) top view of the doped Fe-bcc(100) model. The Fe and N are represented by bronze and blue balls, respectively, in the side view figures. In the top view models, the top layer, 2nd layer, and 3rd layer Fe atoms are represented by bronze, dark gray, and white spheres, respectively. The surface dopant and subsurface dopant are represented by purple and pink balls, respectively.

bcc(211) surfaces is enhanced while the inactive Fe-bcc(100) and Fe-bcc(110) facets are minimized. In analogy with the HHTCS approach,³³ we develop here a high-throughput strategy to screen for dopants that maximize the catalytically active surface area. We apply this to Fe-based NP catalysts for the HB process. In particular, we examine 34 possible dopants across the periodic table and identify 16 promising elements, including such nonmetals as Si and such lanthanide elements as Ce, La, and Eu. Combining these results with previous information on catalytic performance, ^{33,45,46} we select the two most promising dopants, Si and Ni, that increase both the reaction rate and the active surface area, marking them for future experimental studies. To exemplify and validate our screening strategy, for the most promising Si-doped Fe nanoparticles, we assume a realistic size of ~10 nm, identify the optimal Si content, build the corresponding Wulff construction under reaction conditions, and evaluate catalytic reaction rates at the optimal Si doping level.

RESULTS AND DISCUSSION

Our first goal is to predict the facet distribution of the candidate dopants across the periodic table to determine the changes in surface energy brought about by dopant adsorption and how this distribution affects reshaping. We then introduce a reshaping criterion to determine which dopants energetically prefer to adsorb on the catalytically active facets (in our example, Fe-bcc(111)) with respect to the catalytically inactive ones (in our example, Fe-bcc(100)), which can stabilize an increase in surface area of the (111) at the expense of the (100), thereby promoting catalytic rates. We selected the Febcc(111) surface to test these ideas since single-crystal experiments show it to be the most catalytically active surface, which was confirmed by our previous QM calculations. 43 The Fe-bcc(100) surface is selected to test an inactive surface since it is the most stable surface and dominates the surface area when N adatoms are adsorbed, but it is inactive for HB.3 The simulation models are displayed in Figure 1. In the spirit of hierarchical screening methods, we restricted the analysis to dopants that pass the reshaping criterion. Then to this restricted set, we apply a stability or surface propensity criterion. Then to this further restricted set, we apply a

HHTCS criterion to assess the increase in catalytic efficiency. This screening process finds that Si and Ni are the most promising candidates out of the 34 tested. Since Si is predicted to be best, we assess and discuss the Si case in full detail.

Facet Propensity for Dopants and NP Reshaping. The driving force and basic foundation of nanoparticle reshaping is minimizing free energy of the NP, which we use as the guiding principle for our high-throughput screening. For pure systems, the energy minimization criteria can be conveniently expressed in terms of surface energies. However, for multicomponent NP it is more straightforward to use site propensity of the dopant elements, which we quantify in terms of migration energies. That is the energy difference resulting from moving the dopant element between different sites of the nanoparticle. At a given NP composition, the dopant elements will distribute over the structural framework in a combinatorial number of "homotopic" patterns. 9,24 The quantities determining this site propensity are the migration energies, i.e., the energy difference between the various homotops. Focusing for definitiveness on the dopant (X) distribution between N-covered Fe-bcc(111) vs Fe-bcc(100) facets, the (100) \rightarrow (111) dopant migration process reads

migration
$$\equiv \text{Fe}(100)_{\text{X}}(2\text{N}) + \text{Fe}(111)_{\text{p}}(4\text{N})$$

 $\rightarrow \text{Fe}(100)_{\text{p}}(2\text{N}) + \text{Fe}(111)_{\text{X}}(4\text{N})$ (1)

$$\Delta E_{\text{migr}}[N] = E[\text{Fe}(111)_{X}(4N)] + E[\text{Fe}(100)_{p}(2N)] - E[\text{Fe}(100)_{X}(2N)] - E[\text{Fe}(111)_{p}(4N)]$$
(2)

Here we assume that the experimental conditions are such that the Fe surfaces are saturated with N-adatom species, corresponding to the Fe(100)(2N) and Fe(111)(4N) configurations of Figure 1. His is based on the detailed mechanistic studies reported in previous papers. His without dopant, we found previously that Fe(100) $_p$ (2N) and Fe(111) $_p$ (4N) are N-covered Fe facets. However, for the X dopant, we find that Fe(100) $_x$ (2N) and Fe(111) $_x$ (4N) are the N-covered Fe facets. Here the X dopant migrates from the Febcc(100) facet to the Fe-bcc(111) facet in eq 1, leading to

corresponding energetics: the $\Delta E_{\rm migr}[N]$ migration energy, eq 2. Note that, for the moment, we limit eq 2 to the electronic energy. If the dopant prefers a given facet, it will stabilize that facet, decreasing its surface energy with respect to others, *i.e.*, increasing its relative fraction at the expense of Fe-bcc(100) with respect to the pure (undoped) system in the Wulff construction. We then define a reshaping screening criterion that requires $\Delta E_{\rm migr}[N]$ to be negative, *i.e.*, we require that X satisfies the condition:

$$\Delta E_{\text{migr}}[N] < 0 \tag{3}$$

It is important to note that eq 2 also allows the case in which the dopants increase the surface energy of the (111) facet, as long as it is by less than the increase for the (100) facet.

Clearly, we can also define the corresponding migration energy quantity for bare Fe surfaces, i.e.,

$$\Delta E_{\text{migr}}[b] = E[\text{Fe}(100)_{p}(b)] + E[\text{Fe}(111)_{X}(b)]$$

$$- E[\text{Fe}(100)_{X}(b)] - E[\text{Fe}(111)_{p}(b)]$$
(4)

where $\operatorname{Fe}(100)_{X}(b)$, $\operatorname{Fe}(111)_{p}(b)$, $\operatorname{Fe}(100)_{p}(b)$, and $\operatorname{Fe}(111)_{X}(b)$ are bare surfaces of doped (100), pure (111), pure (100) and doped (111), respectively, and the $E[\ldots]$ are the total energies of the corresponding systems. This bare surface energy is useful to predict reshaping under vacuum, making it of interest for experimental validation studies in ultrahigh vacuum (UHV).

Figure 2 displays the transition metal (TM) dopants in the periodic table considered for this analysis. Nontransition metal

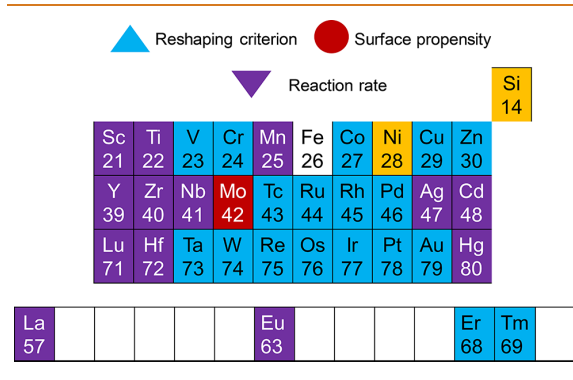


Figure 2. Dopants considered in this work are colored according to the screening criteria for their exclusion, as illustrated in the inset: blue for the reshaping criterion, red for the surface propensity criterion, violet for the HHTCS criterion, leaving two promising dopant (colored in orange) possessing site stability that we expect to produce enhanced catalytic rates both in terms of decreased energy barriers and increased area of catalytically active facets.

(NTM) elements were also considered in previous work, but we include here only Si since it was the only one effective in improving the reaction rate over the Fe-bcc(111) surface out of 18 NTM elements.⁴⁶

Table 1 lists the computed $\Delta E_{\rm migr}[N]$ for the promising dopants that satisfy eq 2. The raw energy data of all the dopants are in the Supporting Information. We found that 16 doping elements satisfy eq 3, which are expected to increase their fraction of the Fe-bcc(111) surface for the NP. Note that some lanthanide elements, Ce, La, and Eu, are very promising to promote Fe-bcc(111) vs Fe-bcc(100). These predictions

can be interesting in two ways: first, they could be tested experimentally to validate the accuracy of the DFT predictions, and second, they could be exploited experimentally to control the growth of Fe nanoparticles, since the surface energy and related adsorption phenomena are known to affect the differential growth rate of the various facet orientations. 50–52

To this end, the energetics of bare facets, *i.e.*, without any adsorbate, are of interest when growth is carried out experimentally in a vacuum; Table S1 reports the computed $\Delta E_{\rm migr}[b]$.

We note that dopants not satisfying eq 3 might conceivably still lead to an increased fraction of the Fe-bcc(111) surface. This could happen if Fe-bcc(100) is the most favorable position of the dopant, but the presence of the dopant decreases the N-adsorption energy on Fe-bcc(100) more than it decreases N-adsorption on other catalytically active facets, making surface doping more favorable than segregation of the dopant into the bulk. We did not find examples of this behavior in the present study.

Surface Propensity (Surface Segregation). To be effective in stabilizing active surfaces, we require that the dopants remain preferentially in the surface or sublayer sites rather than segregating into the bulk. Therefore, our second criterion is surface νs bulk propensity criterion, which is formulated as

$$\Delta E\{\text{Fe-slab} + 2 \times \text{Fe}_{15}\text{-bulk}_X$$

$$\rightarrow \text{Fe-slab}_X + 2 \times \text{Fe}_{16}\text{-bulk}\}$$

$$< 0 \tag{5}$$

where Fe-slab X and Fe-slab represent the slab models of the bare Fe surfaces, Fe-bcc(100), or Fe-bcc(111), with and without dopants, respectively, while Fe16-bulk and Fe15-bulk X are the models of bcc Fe crystal with 16 atoms either pure or and with one Fe atom replaced by one dopant embedded in the crystal, respectively. Here we used the Fe-bcc(100) and Febcc(111) slab energies to apply this criterion, with the results listed as migration energies from bulk to the surface in Table 1. The bare slab is used in this criterion since we want to ensure that the dopants are positioned in the appropriate sites during the synthesis process (in which bare surfaces are typically involved). Naturally, we also want to ensure that no inverse segregation effects occur under reaction conditions. Some dopants, such as Cr, Ni, and Si, are more stable on the top surface for bare Fe(100) than the sublayer surface, while they are more stable in the sublayer as N is adsorbed. In this connection, we note that increasing the doping level toward bulk saturation may be needed to disfavor segregation into the

Within the 16 elements from step (1), 15 elements satisfy eq 5. Only Mo dopant is excluded since Mo prefers to go into the bulk.

Reaction Rate Improvement. We then intersected the candidates screened by the previous two criteria with a "reaction rate improvement" criterion, requiring that the doped facets that are increased in area are also more catalytically active (here we use our rate estimates based on our previous HHTCS studies of resulting catalytic performance). ^{33,45,46} Among the 15 elements in our previous screening, only Si and Ni satisfy this last criterion of increased catalytic rates. In addition to a preference for locating at subsurface of Febcc(111) rather than on Fe-bcc(100) or in bulk Fe, we

Table 1. Fe-bcc(100) \rightarrow Fe-bcc(111) Migration Energies for N-Covered Surfaces, $\Delta E_{\text{migr}}[N]$, for the Various Dopants That Satisfy Equation 2, Corresponding N-Adsorption Energies on bcc(100) and bcc(111) Facets, and Migration Energy from the Bulk to the Bare bcc(100) and bcc(111) Surfaces^a

elements	N-binding on Fe- bcc(100) (eV)	N-binding on Fe- bcc(111) (eV)	$\Delta E_{ ext{migr}}[ext{N}] \ (ext{eV})$	dopant migration energy (eV) from bulk to Fe-bcc(100)	dopant migration energy (eV) from bulk to Fe-bcc(111)
Ce	24.463	23.379	-2.289	-5.572	-3.640
La	24.253	22.324	-2.255	-9.046	-8.981
Eu	23.938	27.426	-1.912	-9.189	-8.233
Y	24.678	22.007	-1.503	-7.283	-7.524
Hg	19.712	19.674	-1.175	-5.410	-5.024
Lu	24.601	21.887	-1.067	-5.908	-5.876
Mo	25.732	21.981	-0.730	1.027	0.452
Zr	25.402	21.897	-0.515	-2.794	-2.991
Sc	25.335	21.953	-0.510	-3.696	-3.711
Si	23.908 (sub)	20.573 (sub)	-0.459	-0.730	-0.842
Hf	25.538	21.967	-0.292	-2.077	-2.048
Cd	21.061	19.905	-0.185	-5.197	-4.707
Mn	23.939	21.044	-0.151	-1.054	-1.131
Ni	24.214 (sub)	20.653 (sub)	-0.063	-0.766	-1.022
Ti	25.824	21.905	-0.054	-0.282	-0.427
Nb	25.698	21.698	-0.051	-0.225	-0.653
Fe	24.228	21.152	0	0	0

[&]quot;Details discussed in the Surface Propensity (Surface Segregation) section. The N-adsorption energy is computed using the bare surface and N_2 molecule as the reference state.

assessed the effect of these dopants on performance for the Febcc(111) surface by reconstructing the full reaction energy network for the doped surface followed by explicit kMC simulations of catalytic rates. This predicted an increase of TOF of $\sim\!42$ -fold for Si and $\sim\!20$ -fold for Ni, at reduced HB conditions of 400 °C/20 atm. 45,46 This makes Si and Ni the most promising dopants among all 34 elements examined. In this paper, we focused only on the most promising dopant Si (also the most promising dopant among all the initial candidates), which prefers Si subsurface on Fe-bcc(111). This is the topic for the next subsection.

Dynamic Wulff Construction for Pure and Si-Doped Fe Systems. First, we examine the surface site stability of Si under HB conditions, which is the optimal location of Si in the various sites of Fe-bcc(111) facets covered by NH_x (x = 1 or 2 or 3) and H absorbed species in the HB reaction. We choose 400 °C/20 atm total reactant pressure and 1 atm NH₃, which have been investigated as realistic target operating conditions for a much less energy-demanding HB process. Using results from our previous work,46 we find that the 3N.NH3 configuration is more appropriate for our analysis than the 4N configuration considered above: it is the dominant configuration based on kMC actual populations under HB and 400 °C/20 atm-reactant/1 atm-NH₃ conditions. It significantly more populated (60.4% of residence time under steady-state) and therefore more representative than the 4N state (1.6% of residence time). Focusing on the 3N.NH3 configuration, we compared the energy of configurations with Si located at a sublayer site or in the fifth layer (to represent Si segregation to the bulk). Our DFT calculations find that Si in the sublayer site is more stable that Si in the fifth layer by 0.591 eV for the 13-layer slab model, providing a value for the bulk migration energy. Since the 3N.NH₃ configuration is more stable under the chosen conditions than the 4N by 0.655 eV per (2×2) surface, we simply add this term to the $Fe-bcc(100) \rightarrow Fe-bcc(111)$ facet migration energy, $\Delta E_{\text{migr}}[N]$, of Table 1. Similarly, we calculate the Febcc(110) → Fe-bcc(111) and Fe-bcc(211)R(missing row reconstruction²³) \rightarrow Fe-bcc(111) facet migration energies for the 3N.NH₃ configuration for bcc(111), which are 0.550 and 1.245 eV, respectively. We note that, although the unreactive (100) and (110) surfaces retain their resting state configurations irrespective of reaction conditions, the free energies of the various configurations of the reactive surfaces and their relative populations depend upon the thermodynamic chemical potentials of reactants and products even under the noreaction assumption. For example, the 3N.NH₃ configuration depends on the steady-state pressures of both N2 and NH3. Thus, the relative stability of Fe-bcc(111) with respect to the other facets depends on the progress of the HB reaction, becoming more dominant and more stable as the reaction proceeds even assuming a constant pressure of reactants. This also affects the site preference for Si since subsurface to Febcc(111) is a more favored location for Si under a very wide set of conditions, but bulk segregation becomes favored by 0.06 eV in the limit of zero NH3 pressure. This transition in site preference to the bulk occurs when the NH3 pressure becomes lower than 0.03 Torr, which occurs at the very beginning of the HB process. On the other reactive surface, Febcc(211)R, the maximally populated configuration is 3N.NH₂, which also depends on the product pressure (on the progress of the reaction).

We now work in the semigrand-canonical thermodynamic ensemble, *i.e.*, in the canonical ensemble for Si and Fe, corresponding to some given loading of Si from deposition experiments, while we work in the grand canonical ensemble for the gas-phase species. In other words, we assume that at a fixed Si composition and with a given size of nanoparticles of about 10 nm in diameter (a size similar to that estimated for the industrial catalyst, see the estimate of paracrystallinity in S16-18 of ref 53), we assume that the nanoparticles are able to reshape during the experimental reaction times according to the Wulff construction (this is reasonable since experimental reaction times are many hours). Here we seek to find the ideal

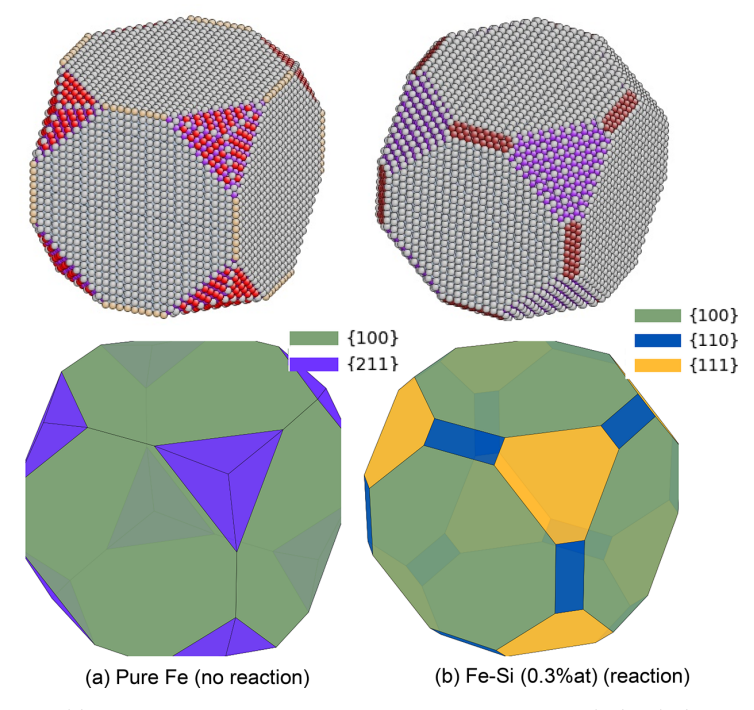


Figure 3. Wulff construction for (a) pure-Fe nanoparticles under no-reaction conditions of $P(H_2)$, $P(N_2) = 15$, 5 atm, T = 673 K and (b) optimally Si-doped nanoparticles under reaction conditions of $P(H_2)$, $P(N_2)$, $P(N_3) = 15$, 5, 1 atm, T = 673 K. The atoms in atomistic figures are color coded by coordination number (CN, the CN2, CN4, CN5, CN6, CN7, CN8 are represented by burly wood, gray, red, brown, purple, and light steel blue balls, respectively). Here blue is (110), gold is (111), green is (100), and purple is (211)R Fe surfaces, respectively.

Si composition that optimizes the overall efficiency of the HB process

We start from pure Fe particles at their optimal Wulffconstruction shape and progressively replace Fe with Si atoms. Given the significant preference of Si for the subsurface site on Fe-bcc(111), we assume that Si atoms fed into the system will especially occupy these Fe-bcc(111)-subsurface sites, neglecting for the moment the Boltzmann distribution. At very low Si atomic content, all subsurface-(111) sites will quickly become 25%-saturated since the Fe-bcc(111) facets have very low area in the optimal Wulff-construction shape for undoped Fe nanoparticles, see Figure 3a. If the particle shape is frozen, any additional Si dopants will go into the second most favorable site, the bulk sites. It is important to note that the bulk \rightarrow (100) migration energy is positive 0.774 eV for Si subsurface under N-covered conditions, whereas for the bare Fe-bcc(100) surface, the bulk site is preferred. The reason is that for the Fe(111) surface, the dominant configuration is 3N.NH₃, in which the subsurface Si is located under NH3 (with which repulsion is minimal), so that this subsurface site is more favorable compared to the bulk. This indicates that second most favorable site for Si doping is the bulk under reaction conditions. However, if the area of the other facets, such as the dominant Fe-bcc(100) facets, is reduced in favor of that of the Fe-bcc(111) facets, there will be additional subsurface Febcc(111) sites available for Si doping so that the system will achieve an energy gain by reshaping to a new Wulff construction while moving Si atoms from bulk sites to these new subsurface-(111) sites, an energy gain precisely given by the bulk \rightarrow (111) migration energy. This phenomenon can be

modeled by selectively decreasing the Fe-bcc(111) surface energy by subtracting the bulk migration energy in the Wulff construction. By recalculating the Wulff shape with this decreased Fe-bcc(111) surface energy, we find that the area of the Fe-bcc(111) facets will be significantly increased, as shown in Figure 3b, and that a Si atomic content of 0.3% is sufficient to saturate all the possible (111)-subsurface sites in the newly reshaped nanoparticles. Table 2 reports the surface free-energies of pure Fe facets and Fe-bcc(111)-Si-doped facets evaluated according to the described procedure in methodology, while Figure 3 illustrates the Wulff shapes of

Table 2. Surface Free-Energies of Pure and 0.3%-Si-Doped Particles of \approx 10 nm in Diameter under 400°C/20 atm-Reactants/1 atm-NH₃ Conditions^a

surface/ configuration	pure-Fe no-reaction H_2 , N_2 = 15,5; $T = 673$ K	Si-doped 0.3% reaction $H_2N_2NH_3 = 15,5,1; T = 673 \text{ K}$
100-2N	1.762 [1.636]	1.896
110-1N	2.517 [2.374]	2.468
111-4N	2.538	2.356 (2.550)
211R-4N	2.369 [2.261]	2.611 (2.636)

a The surface energy of Si-doped Fe-bcc(111) is calculated using the $3N.NH_3$ dominant configuration and modulated by subtracting the Fe-bcc(111) ← bulk migration energy, while that of Fe-bcc(211)R is calculated using the $3N.NH_2$ dominant configuration, with the original surface energies in parentheses, as discussed in the text. The values in brackets is the accurate values from phonon calculation considering the relaxation of all atoms in the slab model. The surface energy ratios are different by \sim 2% comparing the estimation and accurate values, validating the accuracy of estimation.

pure and 0.3%-Si-doped Fe particles under 400 °C/20 atmreactants/1 atm-NH3 conditions. Note that we have calculated the Fe-bcc(111) surface energy by assuming that Fe-bcc(111) is in the 3N.NH₃ dominant configuration. This corresponds to defining "steady-state" surface free-energies in the Wulff construction and thus arriving at a "Wulff construction under steady-state" or "dynamic Wulff construction". 20,21,23 We add that a doping content higher than the ideal estimate given above (i.e., around 0.5%) can be used in an actual experiment to compensate for part of the Si dopant lost into bulk sites according to the Boltzmann distribution. By combining this reshaping effect with the fact that the activity of Si-subsurface doped Fe-bcc(111) facets is far greater than that of the catalytically active facets of pure Fe nanoparticles by a factor of ≈42 (we recall that Fe-bcc(111) and Fe-bcc(211)R have a nearly identical activity per (2×2) surface site), we find that, under the chosen conditions, the promoting or enhancement effect of optimal Si doping corresponds to an enhancement factor of ≈ 56 in the HB catalytic activity per nanoparticle. It is interesting to note that the area of (111) facets may be increased by Si doping at a subsaturation level. Indeed, even at very low Si doping levels, there is an energy gain in slightly increasing the area of the (111) facets with respect to (100) facets while allowing the Si dopant to distribute among all the sites of these increased (111) facets. However, we focus here on the supersaturation level because our goal is to optimize catalytic performance, which is achieved when (111) facets are both as large as possible and also Si-doped.

We could further tune our modeling by taking better account of the actual state of the catalyst surface under reaction conditions without going into a full kMC simulations of the real nanoparticles. To this end, we could calculate the steady-state surface energetics in the following way. We take the populations of the various configurations from kMC simulations under the given steady-state conditions. Here we denote P_i as the population of the *i*th-state (*i.e.*, the percent of time spent by the system on the given configuration under steady-state as derived from the kMC run). Then, as done previously,⁴¹ taking a given zeroth-state as a reference, we define the difference in free-energy of the *i*th-state with respect to the reference zeroth-state, δG , as follows: $\delta G = -k_{\rm B}T \ln(P_i/P_i)$ P_0), and we add this difference to the free-energy of the zerothstate to obtain steady-state free-energies under reaction conditions. We could then use these free-energies weighted by the P_i values to calculate the steady-state average energy of the catalytic facet in the steady-state reaction process under the given thermodynamic conditions and finally tune the average surface energies by the Si migration energies as discussed before. In the present case, however, there is no appreciable effect on the results with respect to considering only the 3N.NH₃ dominant configuration.

Before going to the conclusions, we note that the catalytic system we consider here (Fe-based nanoparticle catalysts in the HB process) is on the too-strong adsorption slope of the volcano curve. ⁵⁴ That is Fe adsorbs nitrogen adatoms (N) too strongly, thus requiring too large an energy penalty to transform its (111) facets from, say, the catalytically inactive 4N configuration to the 2N configuration that has nearestneighbor empty sites to absorb and dissociate gas-phase N₂. ^{41,42} This means that dopants on Fe-based catalysts aimed at increasing HB efficiency are expected to decrease the adsorption energy of nitrogen on the surfaces (so as to get closer to the volcano peak), which implies decreasing the

stabilization brought about by N adsorption and simultaneously to energetically stabilize the catalytically active facet with respect to both the inactive facets and the bulk (at least at the optimal doping level). These are stringent constraints, but Si subsurface to bcc(111) is able to satisfy them, as shown above. Clearly, quantitatively more important and more spectacular effects can be expected in general terms for catalysts on the too-weak adsorption slope of the volcano curve. Here the dopant would be expected to increase the N-adsorption energy, likely leading to a decrease in surface energy of the reactive facets and therefore to a more spectacular increase in their relative areas.

CONCLUSIONS

In summary, we propose to manipulate the shape of nanoparticles through doping combined with chemisorption and catalysis. The Fe-based catalyst for HB process was taken as the specific example to illustrate the principles aimed at improving the catalytic rates. Our predictions on the reaction mechanism for HB reduction of N_2 to NH_3 and validation of the predictions by comparing to single crystal experiments, with excellent agreement on the TOF for the best two surfaces, (111) and (211). This set the stage for the next step of determining the optimum dopants, where to dramatically cut the computational costs, we developed the hierarchical *in silico* optimization of dopants that maximize rates.

In this paper, we take a further step of developing the best possible catalyst by optimizing the NP shape. We examined the relationship between catalytic efficiency of NPs and catalyst composition from adding dopant elements. Considering the HB catalytic reactions on Fe nanoparticles, we proposed and tested the HHTCS approach to screening toward the dopants most promising to increase the surface area of active surface orientation at the expense of inactive surfaces. Using site propensity of the dopant elements, which we quantify in terms of migration energies, we were able to sift out the most promising dopants to most significantly improve catalytic performance. This HHTCS process identified Ni and Si as the best two candidates. Finally, we performed steady-state dynamical Wulff construction of Fe bcc nanoparticles with Si dopants at reaction conditions. Compared with the pure Fe nanoparticle, the active Fe-(111) surface is significantly increased by doping a small amount of Si (~0.3%), leading to a rate enhancement of 56 per nanoparticle under reduced HB conditions. This approach provides an effective way to search for the NP with significantly improved catalytic performance.

METHODS

Surface, adsorption and homotops' energetics were computed using slab models and density functional theory (DFT) predictions. Figure 1a,b,d,e displays the slab models used: 11 layers for Fe-bcc(100) and 13 layers for Fe-bcc(111) surfaces, together with two important N-adsorption configurations. Figure 1c,f depicts top-layer and subsurface-layer doping sites for these two surfaces. In the slab models, only one layer, the middle layer, is fixed while other 10 or 12 layers are allowed to relax to optimum atom positions. The larger thickness of the slab compared to previous works⁴¹ is needed to estimate accurate surface energies.⁵⁵ A vacuum of at least 15 Å is used in the slab models to minimize interactions between periodic images. Dopants were added by replacing the surface or subsurface Fe atoms as illustrated in Figure 1c,f. To maintain the symmetry in the slab model, dopants were introduced in both top and bottom surfaces.

All DFT calculations were carried out using the VASP DFT software using plane-wave basis sets to describe the electronic wave function. Software using plane-wave basis sets to describe the electronic wave function. Software described the Perdew-Burke-Ernzerhof (PBE) exchange and correlation (xc-) functional, Software based on the generalized gradient approximation (GGA). The 3p°3d²4s¹ electrons of Fe were treated explicitly (small core pseudopotential), while the remaining core was described using the projected-augmented-wave approach. The tetrahedron method with Blöchl corrections was used to account for electron partial occupancies. van der Waals interactions were included in the total energy using the D3 corrections with Becke-Johnson (BJ) damping. All calculations allow spin-polarization. Indeed these calculations predict reasonable magnetic moments for the Fe atoms: 2.2 Bohr magnetons for bcc Fe. 4.

A Γ -centered mesh approach was used to sample the first Brillouin zone in reciprocal space with 4 \times 4 \times 1 K-points in all slab models. The energy cutoff for plane wave expansion was 600 eV, the energy convergence of self-consistent field (SCF) was 10^{-6} eV, and the force convergence for ion relaxation was 10^{-3} eV/Å.

The N_2 gas phase energy is taken from previous work using the same computational parameters.⁴¹ The present computational setup has been shown to provide an accurate description of the HB reaction network on Fe-bcc(111) and Fe-bcc(211) reconstructed surfaces.^{41,23}

The surface energy was computed using equation:

$$E_{\text{surface}} \equiv (E_{\text{slab}} - E_{\text{bulk}} - E_{\text{abs}}) / (\text{area})$$
 (6)

where $E_{\rm slab}$, $E_{\rm bulk}$, $E_{\rm abs}$, and area are the energy of the slab model, the energy of the bulk system with the same number of atoms as the slab, the energy of the absorbate, and the area of both the top and bottom surfaces. For the pure Fe slab, we used $E_{\rm bulk} = N \times E_{\rm bcc_atom}$, where N is the number of atoms and $E_{\rm bcc_atom}$ is the atomic energy in BCC Fe. For the doped slab, a bulk alloy system with the same number of atoms was constructed to compute $E_{\rm bulk}$.

To obtain the free energy at finite temperature, we correct the surface energy by calculating the phonon modes and using the harmonic approximation in the partition function to predict free energy. To obtain the phonon modes, we use the finite displacement approach implemented in phonopy, ⁶³ which were then used to compute the vibrational entropy as a function of temperature. ⁶⁴

In evaluating the surface adsorption rate at reaction conditions, we used a simplified approach in which no phonon corrections were employed, and the translational and rotational free energies of the gas phase species were included. We validated this approach by comparing with the phonon calculations with all atoms relaxed for several surface configurations. The details of phonon calculations are in the Supporting Information text and Table S2.

ASSOCIATED CONTENT

Supporting Information

The Supporting Information is available free of charge at https://pubs.acs.org/doi/10.1021/acsnano.0c09346.

Details of phonon calculations, Table S1 displaying the $\Delta E_{\rm migr}[b]$ quantities, and Table S2 showing the convergence of K-points setup in the phonon calculations (PDF)

Raw DFT data for HHTCS (XLSX)

AUTHOR INFORMATION

Corresponding Authors

Qi An — Department of Chemical and Materials Engineering, University of Nevada-Reno, Reno, Nevada 89577, United States; orcid.org/0000-0003-4838-6232; Email: qia@

Alessandro Fortunelli – Materials and Process Simulation Center (MSC), California Institute of Technology, Pasadena, California 91125, United States; CNR-ICCOM, Consiglio Nazionale delle Ricerche, ThC²-Lab, Pisa 56124, Italy; orcid.org/0000-0001-5337-4450; Email: alessandro.fortunelli@cnr.it

William A. Goddard III — Materials and Process Simulation Center (MSC), California Institute of Technology, Pasadena, California 91125, United States; ● orcid.org/0000-0003-0097-5716; Email: wag@caltech.edu

Author

Molly McDonald — Department of Chemical and Materials Engineering, University of Nevada-Reno, Reno, Nevada 89577, United States

Complete contact information is available at: https://pubs.acs.org/10.1021/acsnano.0c09346

Notes

The authors declare no competing financial interest.

ACKNOWLEDGMENTS

M.M. was supported by NSF (Grant CMMI-1727428). A.F. gratefully acknowledges the contribution of the International Research Network IRN on Nanoalloys (CNRS). W.A.G. III thanks ONR (Grant N00014-18-1-2155) for support. The authors would like to acknowledge the support of Research & Innovation and the Cyberinfrastructure Team in the Office of Information Technology at the University of Nevada, Reno for facilitation and access to the Pronghorn High-Performance Computing Cluster.

REFERENCES

- (1) Laurent, S.; Forge, D.; Port, M.; Roch, A.; Robic, C.; Vander Elst, L.; Muller, R. N. Magnetic Iron Oxide Nanoparticles: Synthesis, Stabilization, Vectorization, Physicochemical Characterizations, and Biological Applications. *Chem. Rev.* **2010**, *110*, 2574–2574.
- (2) Dreaden, E. C.; Alkilany, A. M.; Huang, X.; Murphy, C. J.; El-Sayed, M. A. The Golden Age: Gold Nanoparticles for Biomedicine. *Chem. Soc. Rev.* **2012**, *41*, 2740–2779.
- (3) Ramacharyulu, P. V. R. K.; Muhammad, R.; Praveen Kumar, J.; Prasad, G. K.; Mohanty, P. Iron Phthalocyanine Modified Mesoporous Titania Nanoparticles for Photocatalytic Activity and CO₂ Capture Applications. *Phys. Chem. Chem. Phys.* **2015**, *17*, 26456–26462.
- (4) Mansha, M.; Khan, I.; Ullah, N.; Qurashi, A. Synthesis, Characterization and Visible-Light-Driven Photoelectrochemical Hydrogen Evolution Reaction of Carbazole-Containing Conjugated Polymers. *Int. J. Hydrogen Energy* **2017**, 42 (16), 10952–10961.
- (5) Shin, W.-K.; Cho, J.; Kannan, A. G.; Lee, Y.-S.; Kim, D.-W. Cross-Linked Composite Gel Polymer Electrolyte Using Mesoporous Methacrylate-Functionalized SiO₂ Nanoparticles for Lithium-Ion Polymer Batteries. Sci. Rep. 2016, 6, 26332.
- (6) Liu, L.; Corma, A. Metal Catalysts for Heterogeneous Catalysis: from Single Atoms to Nanoclusters and Nanoparticles. *Chem. Rev.* **2018**, *118* (10), 4981–5079.
- (7) Ortiz Peña, N.; Ihiawakrim, D.; Han, M.; Lassalle-Kaiser, B.; Carenco, S.; Sanchez, C.; Laberty-Robert, C.; Portehault, D.; Ersen, O. Morphological and Structural Evolution of Co₃O₄ Nanoparticles Revealed by *in Situ* Electrochemical Transmission Electron Microscopy During Electrocatalytic Water Oxidation. *ACS Nano* **2019**, *13* (10), 11372–11381.
- (8) Jiang, Y.; Li, H.; Wu, Z.; Ye, W.; Zhang, H.; Wang, Y.; Sun, C.; Zhang, Z. In Situ Observation of Hydrogen-Induced Surface Faceting for Palladium-Copper Nanocrystals at Atmospheric Pressure. Angew. Chem., Int. Ed. 2016, 55, 12427–12430.
- (9) Ferrando, R.; Jellinek, J.; Johnston, R. L. Nanoalloys: From Theory to Applications of Alloy Clusters and Nanoparticles. *Chem. Rev.* **2008**, *108* (3), 845–910.

- (10) Hemmingson, S. L.; Campbell, C. T. Trends in Adhesion Energies of Metal Nanoparticles on Oxide Surfaces: Understanding Support Effects in Catalysis and Nanotechnology. *ACS Nano* **2017**, *11* (2), 1196–1203.
- (11) Boudart, M. Catalysis by Supported Metals. Adv. Catal. 1969, 20, 153-166.
- (12) Van Santen, R. A. Complementary Structure Sensitive and Insensitive Catalytic Relationships. *Acc. Chem. Res.* **2009**, 42 (1), 57–66
- (13) Wulff, G. On the Question of the Speed of Growth and the Dissolution of the Crystal Layers. *Z. Kristallogr. Cryst. Mater.* **1901**, 34, 449–530.
- (14) Kern, R.; Müller, P. From Wulff Kaishew' Theorem to Nanodots. In *Nanoscale Phenomena and Structures*; Kaschiev, D., Ed.; Academic Publishing House: Sofia, Bulgaria, 2008.
- (15) Tran, R.; Xu, Z.; Radhakrishnan, B.; Winston, D.; Sun, W.; Persson, K.; Ong, S. P. Surface Energies of Elemental Crystals. *Sci. Data* **2016**, *3*, 160080.
- (16) Hansen, P. L.; Wagner, J. B.; Helveg, S.; Rostrup-Nielsen, J. R.; Clausen, B. S.; Topsøe, H. Atom-Resolved Imaging of Dynamic Shape Changes in Supported Copper Nanocrystals. *Science* **2002**, 295 (5562), 2053–2055.
- (17) Stampfl, C.; Soon, A.; Piccinin, S.; Shi, H.-Q.; Zhang, H. Bridging the Temperature and Pressure Gaps: Close-Packed Transition Metal Surfaces in an Oxygen Environment. *J. Phys.: Condens. Matter* **2008**, *20*, 184021.
- (18) Wang, T.; Tian, X.-X.; Yang, Y.; Li, Y.-W.; Wang, J.-G.; Beller, M.; Jiao, H.-J. Coverage-Dependent N₂ Adsorption and Its Modification of Iron Surfaces Structures. *J. Phys. Chem. C* **2016**, 120 (5), 2846–2854.
- (19) Chmielewski, A.; Meng, J.; Zhu, B.; Gao, Y.; Guesmi, H.; Prunier, H.; Alloyeau, D.; Wang, G.; Louis, G.; Delannoy, L.; Afanasiev, P.; Ricolleau, C.; Nelayah, J. Reshaping Dynamics of Gold Nanoparticles under H₂ and O₂ at Atmospheric Pressure. *ACS Nano* **2019**, *13* (2), 2024–2033.
- (20) Molina, L. M.; Lee, S.; Sell, K.; Barcaro, G.; Fortunelli, A.; Lee, B.; Seifert, S.; Winans, R. E.; Elam, J. W.; Pellin, M. J.; et al. Size-Dependent Selectivity and Activity of Silver Nanoclusters in the Partial Oxidation of Propylene to Propylene Oxide and Acrolein: A Joint Experimental and Theoretical Study. *Catal. Today* **2011**, *160* (1), 116–130.
- (21) Wang, Y.; Barcaro, G.; Negreiros, F. R.; Visart de Bocarme, T.; Moors, M.; Kruse, N.; Hou, M.; Fortunelli, A. Adsorption-Induced Restructuring and Early Stages of Carbon-Nanotube Growth on Ni Nanoparticles. *Chem. Eur. J.* 2013, 19, 406–413.
- (22) Roosen, A. R; McCormack, R. P; Carter, W.C. Wulffman: A Tool for The Calculation and Display of Crystal Shapes. *Comput. Mater. Sci.* 1998, 11, 16–26.
- (23) Fuller, J.; Fortunelli, A.; Goddard III, W. A.; An, Q. Reaction Mechanism and Kinetics for Ammonia Synthesis on the Fe (211) Reconstructed Surface. *Phys. Chem. Chem. Phys.* **2019**, *21*, 11444–11454.
- (24) Calvo, F. Nanoalloys: From Fundamentals to Emergent Applications, 2 nd ed.; Elsevier: Amsterdam, The Netherlands, 2020; https://www.sciencedirect.com/book/9780128198476/nanoalloys.
- (25) Zhu, B.; Xu, Z.; Wang, C.; Gao, Y. Shape Evolution of Metal Nanoparticles in Water Vapor Environment. *Nano Lett.* **2016**, *16* (4), 2628–2632.
- (26) Tao, F.; Grass, M. E.; Zhang, Y.-W.; Butcher, D. R.; Renzas, J. R.; Liu, Z.; Chung, J.-Y.; Mun, B.-S.; Salmeron, M.; Somorjai, G. A. Reaction-Driven Restructuring of Rh-Pd and Pt-Pd Core-Shell Nanoparticles. *Science* 2008, 322, 932–934.
- (27) Ringe, E.; Van Duyne, R. P.; Marks, L. D. Wulff Construction for Alloy Nanoparticles. *Nano Lett.* **2011**, *11* (8), 3399–3403.
- (28) Farsi, L.; Deskins, N. A. First Principles Analysis of Surface Dependent Segregation in Bimetallic Alloys. *Phys. Chem. Chem. Phys.* **2019**, 21, 23626–23637.

- (29) Meng, J.; Zhu, B.; Gao, Y. Surface Composition Evolution of Bimetallic Alloys under Reaction Conditions. *J. Phys. Chem. C* **2019**, 123 (46), 28241–28247.
- (30) Divins, N. J.; Angurell, I.; Escudero, C.; Pérez-Dieste, V.; Llorca, J. Influence of the Support on Surface Rearrangements of Bimetallic Nanoparticles in Real Catalysts. *Science* **2014**, *346*, 620–623
- (31) Duan, M.; Yu, J.; Meng, J.; Zhu, B.; Wang, Y.; Gao, Y. Reconstruction of Supported Metal Nanoparticles in Reaction Conditions. *Angew. Chem., Int. Ed.* **2018**, *57*, 6464–6469.
- (32) Piccolo, L. Restructuring Effects of The Chemical Environment in Metal Nanocatalysis and Single-Atom Catalysis. *Catal. Today* **2020**, DOI: 10.1016/j.cattod.2020.03.052.
- (33) An, Q.; Shen, Y. D.; Fortunelli, A.; Goddard III, W. A. QM-Mechanism-Based Hierarchical High-Throughput *in Silico* Screening Catalyst Design for Ammonia Synthesis. *J. Am. Chem. Soc.* **2018**, *140*, 17702–17710.
- (34) Appl, M. Ammonia, Ullmann's Encyclopedia of Industrial Chemistry; Wiley-VCH: Weinheim, Germany, 2006.
- (35) Buijsman, E.; Maas, H. F. M.; Asman, W. A. H. Anthropogenic NH, Emissions in Europe. Atmos. Environ. 1987, 21 (5), 1009–1022.
- (36) Bouwman, A. F.; Boumans, L. J. M.; Batjes, N. H. Estimation of Global NH₃ Volatilization Loss from Synthetic Fertilizers and Animal Manure Applied to Arable Lands and Grasslands. *Global Biogeochem. Cycles* **2002**, *16* (2), 8-1–8-14.
- (37) Jennings, J. R. Catalytic Ammonia Synthesis: Fundamentals and Practice; Plenum Press: New York, 1991.
- (38) Mittasch, A. Early Studies of Multicomponent Catalysts. *Adv. Catal.* **1950**, *2*, 81–104.
- (39) Ertl, G. Elementary Steps in Heterogeneous Catalysis. *Angew. Chem., Int. Ed. Engl.* **1990**, 29, 1219–1227.
- (40) Gambarotta, S.; Scott, J. Multimetallic Cooperative Activation of N₂. Angew. Chem., Int. Ed. **2004**, 43, 5298–5308.
- (41) Qian, J.; An, Q.; Fortunelli, A.; Nielsen, R. J.; Goddard III, W. A. Reaction Mechanism and Kinetics for Ammonia Synthesis on the Fe(111) Surface. *J. Am. Chem. Soc.* **2018**, *140*, 6288–6297.
- (42) Mortensen, J. J.; Hansen, L. B.; Hammer, B.; Nørskov, J. K. Nitrogen Adsorption and Dissociation on Fe(111). *J. Catal.* **1999**, 182, 479–488.
- (43) Somorjai, G. A.; Materer, N. Surface Structures in Ammonia Synthesis. *Top. Catal.* **1994**, *1*, 215–231.
- (44) Strongin, D. R.; Carrazza, J.; Bare, S. R.; Somorjai, G. A. The Importance of C7 Sites and Surface Roughness in the Ammonia-Synthesis Reaction over Iron. *J. Catal.* **1987**, *103*, 213–215.
- (45) Mcdonald, M.; Fuller, J.; Fortunelli, A.; Goddard III, W. A.; An, Q. Highly Efficient Ni-Doped Iron Catalyst for Ammonia Synthesis from Quantum-Mechanics-Based Hierarchical High-Throughput Catalyst Screening. *J. Phys. Chem. C* 2019, 123, 17375–17383.
- (46) An, Q.; Mcdonald, M.; Fortunelli, A.; Goddard III, W. A. Si-Doped Fe Catalyst for Ammonia Synthesis at Dramatically Decreased Pressures and Temperatures. *J. Am. Chem. Soc.* **2020**, *142*, 8223–8232.
- (47) Fuller, J.; Fortunelli, A.; Goddard III, W. A.; An, Q. Discovery of Dramatically Improved Ammonia Synthesis Catalysts through Hierarchical High Throughput Catalyst Screening of the Fe(211) Surface. *Chem. Mater.* **2020**, 32 (23), 9914–9924.
- (48) Rayment, T.; Schlogl, R.; Thomas, J. M.; Ertl, G. Structure of the Ammonia Synthesis Catalyst. *Nature* **1985**, *315*, 311–313.
- (49) Bozso, F.; Ertl, G.; Grunze, M.; Weiss, M. Interaction of Nitrogen with Iron Surfaces: I. Fe(100) and Fe(111). *J. Catal.* **1977**, 49, 18–41.
- (50) Chernov, A. A. The Kinetics of the Growth Forms of Crystal. Sov. Phys. Crystallogr. 1963, 7, 728–730.
- (51) Heyer, H. The Kinetics of Crystal Growth. Angew. Chem., Int. Ed. Engl. 1966, 5, 67–77.
- (52) Al-Saidi, W. A.; Feng, H.-J.; Fichthorn, K. A. Adsorption of Polyvinylpyrrolidone on Ag Surfaces: Insight into a Structure-Directing Agent. *Nano Lett.* **2012**, *12* (2), 997–1001.

- (53) Kandemir, T.; Schuster, M. E.; Senyshyn, A.; Behrens, M.; Schlögl, R. The Haber–Bosch Process Revisited: On the Real Structure and Stability of "Ammonia Iron" under Working Conditions. *Angew. Chem., Int. Ed.* **2013**, 52 (48), 12723–12726.
- (\$4) Medford, A. J.; Vojvodic, A.; Hummelshøj, J. S.; Voss, J.; Abild-Pedersen, F.; Studt, F.; Bligaard, T.; Nilsson, A.; Nørskov, J. K. From the Sabatier Principle to a Predictive Theory of Transition-Metal Heterogeneous Catalysis. *J. Catal.* **2015**, 328, 36–42.
- (55) Da Silva, J. L. F.; Stampfl, C.; Scheffler, M. Converged Properties of Clean Metal Surfaces by All-Electron First-Principles Calculations. *Surf. Sci.* **2006**, *600* (3), 703–715.
- (56) Kresse, G.; Hafner, J. Ab Initio Molecular Dynamics for Liquid Metals. Phys. Rev. B: Condens. Matter Mater. Phys. 1993, 47, 558-561.
- (57) Kresse, G.; Furthmüller, J. Efficiency of *ab Initio* Total Energy Calculations for Metals and Semiconductors Using a Plane-Wave Basis Set. *Comput. Mater. Sci.* **1996**, *6*, 15–50.
- (58) Kresse, G.; Furthmüller, J. Efficient Iterative Schemes for ab Initio Total-Energy Calculations Using a Plane-Wave Basis Set. Phys. Rev. B: Condens. Matter Mater. Phys. 1996, 54, 11169–11186.
- (59) Kresse, G.; Joubert, D. From Ultrasoft Pseudopotentials to the Projector Augmented-Wave Method. *Phys. Rev. B: Condens. Matter Mater. Phys.* 1999, 59, 1758–1775.
- (60) Perdew, J. P.; Burke, K.; Ernzerhof, M. Generalized Gradient Approximation Made Simple. *Phys. Rev. Lett.* **1996**, *77*, 3865–3868.
- (61) Perdew, J. P.; Burke, K.; Ernzerhof, M. Erratum: Generalized Gradient Approximation Made Simple. *Phys. Rev. Lett.* **1997**, 78, 1396–1396.
- (62) Johnson, E. R.; Becke, A. D. A Post-Hartree-Fock Model of Intermolecular Interactions: Inclusion of Higher-Order Corrections. *J. Chem. Phys.* **2006**, *124*, 174104.
- (63) Togo, A.; Oba, F.; Tanaka, I. First-Principles Calculations of the Ferroelastic Transition between Rutile-Type and CaCl₂-Type SiO₂ at High Pressures. *Phys. Rev. B: Condens. Matter Mater. Phys.* **2008**, 78, 134106.
- (64) Dove, M. T. Introduction to Lattice Dynamics; Cambridge University Press: Cambridge, U.K., 1993.